ADVANCED OPTICAL MATERIALS
www.advopticalmat.de

Sulfur Vacancy Related Optical Transitions in Graded Alloys of $Mo_xW_{1-x}S_2$ Monolayers

*Mahdi Ghafariasl, Tianyi Zhang, Zachary D. Ward, Da Zhou, David Sanchez, Venkataraman Swaminathan, Humberto Terrones, Mauricio Terrones, and Yohannes Abate**

Engineering electronic bandgaps is crucial for applications in information technology, sensing, and renewable energy. Transition metal dichalcogenides (TMDCs) offer a versatile platform for bandgap modulation through alloying, doping, and heterostructure formation. Here, the synthesis of a 2D $Mo_xW_{1-x}S_2$ graded alloy is reported, featuring a Mo-rich center that transitions to W-rich edges, achieving a tunable bandgap of 1.85 to 1.95 eV when moving from the center to the edge of the flake. Aberration-corrected high-angle annular dark-field scanning transmission electron microscopy showed the presence of sulfur monovacancy, V_S, whose concentration varied across the graded $Mo_xW_{1-x}S_2$ layer as a function of Mo content with the highest value in the Mo-rich center region. Optical spectroscopy measurements supported by ab initio calculations reveal a doublet electronic state of V_S, which is split due to the spin-orbit interaction, with energy levels close to the conduction band or deep in the bandgap depending on whether the vacancy is surrounded by W atoms or Mo atoms. This unique electronic configuration of V_S in the alloy gave rise to four spin-allowed optical transitions between the V_S levels and the valence bands. The study demonstrates the potential of defect and optical engineering in 2D monolayers for advanced device applications.

1. Introduction

Bandgap engineering is of great importance in modern semiconductor technology because of its capability for tuning the materials' optical and electrical properties that are key to their applications. In the past decade, the emergence of atomically thin 2D layered materials has provided an open canvas to engineer their bandgaps for device applications such as tunable lasers, light-emitting diodes (LEDs), and nanoelectronics.[1,2] Among the family of 2D materials,[3–6] monolayers of semiconducting transition metal dichalcogenides (TMDCs), such as MoS_2 and WS_2,[7] possess direct bandgaps at optical frequencies, making them excellent candidates for bandgap engineering via diverse approaches such as alloying, heterostacking, strain engineering, intercalation, temperature control, and applying external electric fields.[8–16] Compared to bandgap tuning approaches that rely on external applied factors (e.g., temperature, strain, and electric field), alloying provides an effective and stable control because the bandgap is controlled by the intrinsic chemical composition, and a continuous bandgap engineering can be achieved by precisely modulating the alloy composition.[17,18] To date, ternary alloys of monolayer TMDCs (e.g., $Mo_xW_{1-x}S_2$, $MoS_{2x}Se_{2(1-x)}$) have been achieved using chemical vapor deposition (CVD)[19,20] physical vapor deposition (PVD),[21,22] exfoliation of bulk crystals synthesized by chemical vapor transport (CVT),[23] and other methods, allowing for the access of tunable optical properties as a function of compositions.

We employed an alkali metal halide-assisted CVD method to synthesize alloyed $Mo_XW_{1-X}S_2$ monolayers that showcase intriguing compositional gradients within individual crystals, and we

M. Ghafariasl, Y. Abate
Department of Physics and Astronomy
University of Georgia
Athens, GA 30602, USA
E-mail: yohannes.abate@uga.edu

The ORCID identification number(s) for the author(s) of this article can be found under https://doi.org/10.1002/adom.202302326

DOI: 10.1002/adom.202302326

T. Zhang, D. Sanchez, M. Terrones
Department of Materials Science and Engineering
The Pennsylvania State University
University Park, PA 16802, USA

Z. D. Ward, H. Terrones
Department of Physics and Astronomy
Rensselaer Polytechnic Institute
Rensselaer, NY 12180, USA

D. Zhou, M. Terrones
Department of Physics
The Pennsylvania State University
University Park, PA 16802, USA

V. Swaminathan
Department of Materials Science and Nanoengineering
Rice University
Houston, TX 77005, USA

thoroughly examined their optical properties. The alloys exhibit distinct compositional gradients transitioning from a Mo-rich center to a W-rich periphery. This strategically controlled alloying within a single crystal enabled significant spatial tuning of the bandgap in the context of 2D TMDC materials, with a notable variation of over 0.1 eV, characterized by a uniform radial emission profile spanning across the entire flake, and facilitated the investigation of continuously composition-dependent intralayer optical transitions. Examining the defect structure in the alloy using aberration-corrected high-angle annular dark-field scanning transmission electron microscopy (AC-HAADF-STEM) showed the presence of sulfur monovacancy, V_S, whose concentration varied across the graded $Mo_xW_{1-x}S_2$ layer as a function of Mo content with the highest value in the Mo rich center region and the lowest value in the W rich edges. Detailed spectral analysis of the photoluminescence from the alloy as a function of temperature (4–300 K) and laser excitation intensity suggested several intralayer optical transitions besides the intrinsic band edge excitons. To investigate the origin of these transitions, detailed ab initio calculations were performed of the band structure of the alloy considering spin-orbit interactions. A doublet electronic state of V_S, which was split due to the spin-orbit interaction, was identified for the first time with energy levels close to the conduction band or deep in the band gap depending on whether the vacancy in the alloy is surrounded by W atoms or Mo atoms. This unique electronic configuration of V_S in the alloy gave rise to four spin-allowed optical transitions between the V_S levels and the valance bands. Matching the calculated transition energies with the peak positions of the deconvoluted peaks, enabled the identification of free-to-bound transitions involving a photoexcited electron captured at the doublet V_S level and a hole in the top of the valence band at k = 0. In addition, bound exciton transitions associated with the V_S doublet were also identified. Thus, a multitude of V_S related intralayer optical transitions reported for the first time in the alloy $Mo_xW_{1-x}S_2$, reveals the complex interplay between composition and defect structure thereby providing the exciting opportunity of the combined defect and optical engineering to realize novel devices in alloyed TMDCs.

2. Results and Discussion

2.1. Sample Synthesis and Characterization

Additive-assisted CVD has recently emerged as a powerful method for the preparation of 2D TMDCs and their heterostructures.[24] The use of growth additives, such as alkali metal halides (e.g., NaCl, NaBr) and organic compounds with aromatic structures (e.g., reduced graphene oxide (rGO), perylene-3,4,9,10-tetracarboxylic acid tetra potassium salt (PTAS), can effectively promote the growth of TMDCs with enhanced yield, increased grain sizes, and improved uniformity of layer numbers and morphology.[25–27] In our work, we employed an additive-assisted synthesis technique to prepare single-crystalline monolayers of alloyed $Mo_xW_{1-x}S_2$. An alkali metal halide-assisted CVD method was applied, with mixed MoS_2 and WO_3 powders as transition metal precursors and NaBr as a growth promoter (**Figure 1a**). An optical image of typical as-grown $Mo_xW_{1-x}S_2$ alloys is displayed in Figure 1b, showing truncated-triangular morphologies with noticeable optical contrast differences from center to edge regions. Unlike the in-plane heterostructures synthesized by liquid-phase precursor-assisted approach, which we previously reported,[28,29] this method produced alloyed $Mo_xW_{1-x}S_2$ monolayers with center-to-edge composition gradient (a schematic is shown in **Figure 2a**). Note that the composition gradient is not only present in $Mo_xW_{1-x}S_2$ monolayers grown by this approach. Instead, graded TMDC alloys including $Mo_xW_{1-x}S_2$ and $MoS_{2(1-x)}Se_{2x}$ have previously been synthesized using different strategies, for example, two-step growth of $Mo_xW_{1-x}S_2$ using MoO_3 and WO_3 precursors, and one-step chalcogenization of ammonium molybdate by mixed S and Se to form $MoS_{2(1-x)}Se_{2x}$.[30–34] The formation of such a center-to-edge composition gradient could be explained by different growth rates of individual TMDC components (e.g., MoS_2 and WS_2) and/or a competence between compositional separation and mixing, which are affected by multiple factors during the CVD process such as the vapor pressure of precursors, growth temperature, substrate, etc. Z-contrast aberration-corrected high angle annular dark field scanning transmission electron microscopy (AC-HAADF-STEM) imaging of the $Mo_xW_{1-x}S_2$ monolayer revealed that the Mo and W concentrations varied continuously from the center to the edge of the flake. The center regions contain a higher Mo concentration compared to the edge regions which are dominated by W with a compositional gradient interface between the two regions. This observation was further confirmed using far-field Raman and photoluminescence (PL) studies as discussed below. AC-HAADF-STEM imaging further identified that V_S is the prevalent point defect in alloyed $Mo_xW_{1-x}S_2$ monolayers, which is labeled by the red-colored circles in Figure 1c–e. The center, interface, and edge regions contain estimated V_S defect densities of 3.3×10^{13}, 2.2×10^{13}, and 4.2×10^{12} cm^{-2}, respectively. We note that there is a relationship between the prevalent transition metal (Mo or W) and the density of V_S. The center, which has the highest Mo concentration, also has the highest density of V_S. In contrast, the edge, which has the highest W concentration, has the lowest density of V_S. In the interface region, between the center and edge regions, we observed a V_S density bounded by the two regions. The V_S densities for the Mo-rich center and W-rich edge regions are in accordance with defect densities previously measured in CVD-grown MoS_2 and WS_2 monolayers.[35,36]

2.2. Optical Characterization of Alloyed $Mo_xW_{1-x}S_2$ at Room Temperature

To characterize the structural and optical properties of as-synthesized TMDC alloys, we performed far-field Raman and PL measurements. Figure 2b,e illustrates the Raman spectra acquired from different regions of $Mo_xW_{1-x}S_2$ alloys. The material exhibits Raman signatures that are consistent with the previous results, with MoS_2-like vibrational modes dominating in center regions and WS_2-like vibrational modes in edge regions, while the interface/middle regions exhibit a combination of both sets of modes.[28,31] The PL emissions from the center (≈1.85 eV) and edge regions (≈1.95 eV) of the alloyed structure are close to the optical band gap of pristine MoS_2 and WS_2, respectively (Figure 2c).

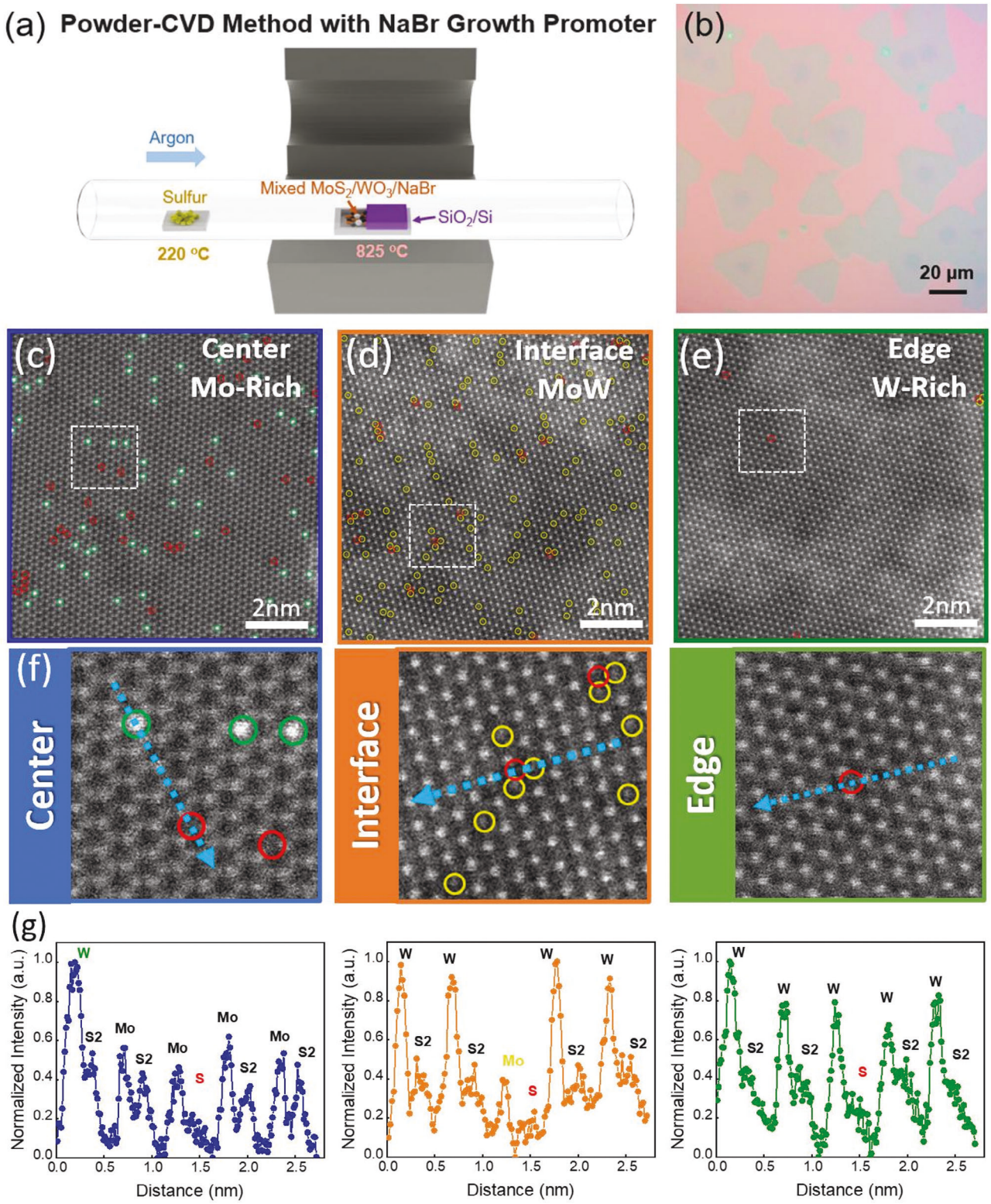

Figure 1. The synthesis of Alloyed $Mo_xW_{1-x}S_2$ and AC-HRSTEM Structural Characterization. a) A schematic of the synthesis of alloyed $Mo_xW_{1-x}S_2$ monolayers with a center-to-edge composition gradient. b) Optical image of as-grown $Mo_xW_{1-x}S_2$ monolayer on SiO_2/Si substrate. c–e) Typical AC-HAADF-STEM images were acquired from the center, interface, and edge areas of the $Mo_xW_{1-x}S_2$ monolayer. The red, green, and yellow circles denote the sulfur monovacancy (V_S), W atoms, and Mo atoms, respectively. f) magnified images of the white dash boxes at the center, interface, and edge areas of the $Mo_xW_{1-x}S_2$ monolayer. g) The corresponding intensity line profiles of areas marked by the blue arrows in f) for three different regions of the alloyed $Mo_xW_{1-x}S_2$ monolayer.

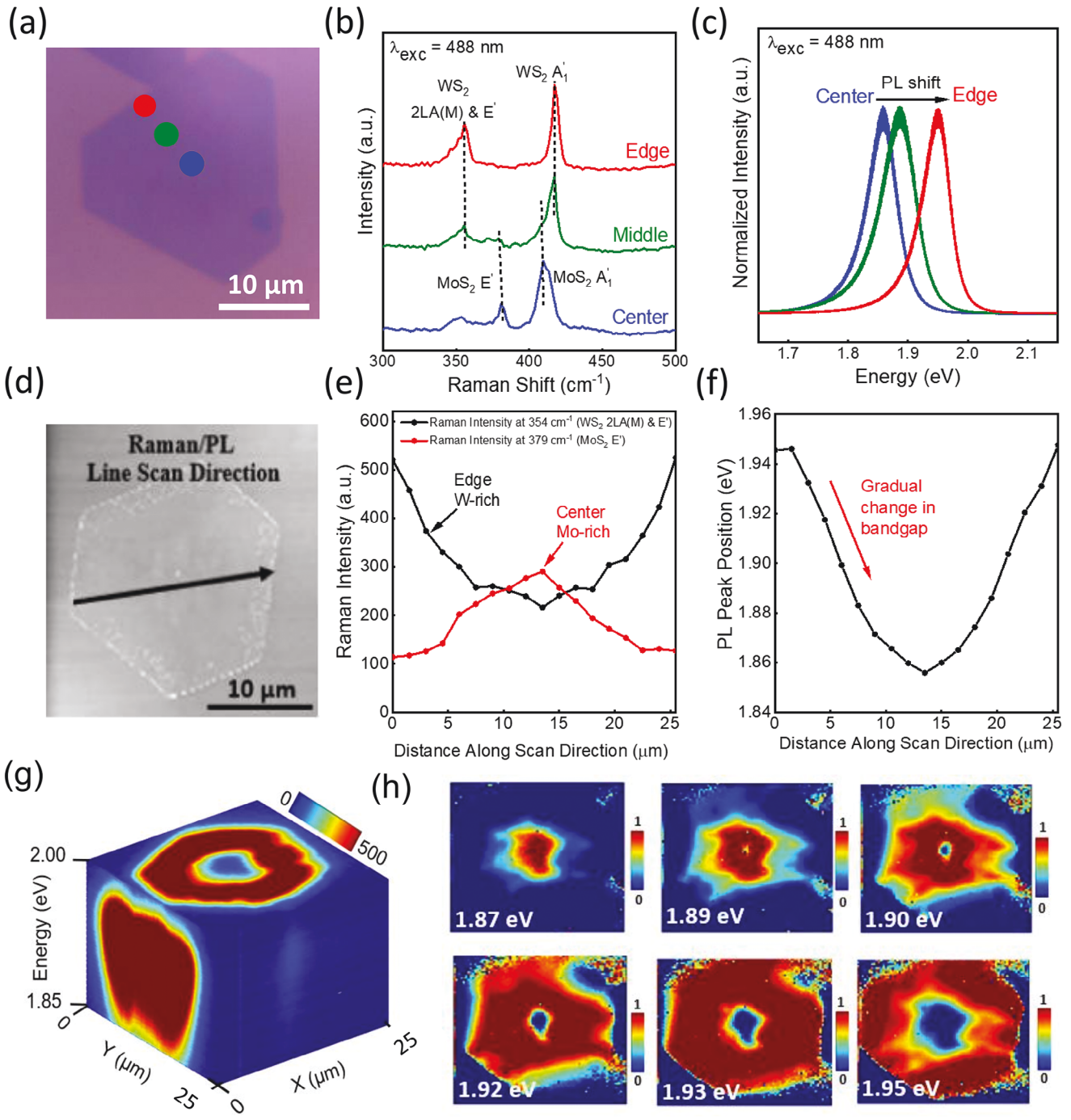

Figure 2. Optical Characterization of alloyed monolayer $Mo_xW_{1-x}S_2$. a) Schematic of the structure of alloyed monolayer $Mo_xW_{1-x}S_2$. b) Raman and c) PL spectra of various regions in alloyed monolayer $Mo_xW_{1-x}S_2$. d) Optical microscopy image of the $Mo_xW_{1-x}S_2$ flake used for Raman and PL line scans (the scan direction is marked by the black arrow). e) Raman intensity profiles of WS_2 E' and 2LA(M) modes (black) and MoS_2 E' mode (red line) as a function of distance along the scan direction. Both Raman modes display gradual changes in the scan direction. f) The evolution of PL peak positions of alloyed monolayer $Mo_xW_{1-x}S_2$ as a function of distance along the scan direction. The gradual shift in the peak position along the scan direction indicates spatially varying optical band gaps within the material. g) 3D cube hyperspectral PL map. h) Section cut images taken from the hyperspectral map at different energies.

To further elucidate the structural and optical property differences of the sample as a function of position within the flake, Raman and PL line scans were performed on a representative alloyed monolayer $Mo_xW_{1-x}S_2$ flake along the scan direction marked in Figure 2d and plotted in Figure 2e,f. The intensities of both the convoluted WS_2 E' and 2LA(M) modes (black line) and the MoS_2 E' mode (red line) display a gradual change along the scan direction (Figure 2e), which unambiguously indicates a composition gradient from center to edge of the flake. Consequently, the optical band gap of the alloyed $Mo_xW_{1-x}S_2$ was continuously modulated due to the lateral variation of the degree of alloying, indicated by the gradual change in PL peak positions (Figure 2f) that is consistent with previous results on graded TMDC alloys.[30,37] We also map the band edge emission spatial profile of the $Mo_xW_{1-x}S_2$ alloy by taking hyperspectral PL imaging.[29] Figure 2g shows a 3D hyperspectral data cube taken by measuring an array of 75 by 75 pixels PL normalized spectra of the alloyed monolayer. The x and y axes of the 3D data cube shown in Figure 2g indicate the plane of the sample surface while the z-axis corresponds to the photon energy axis (1.85–2.0 eV). The acquisition time for each spectrum was 1 s, and the total acquisition time of 2 h per image (see Experimental Section for details). The PL spatial map at a fixed energy is extracted by a cross-section cut of the cube as shown in Figure 2h.

The energy dependent PL emission maps reveal the 2D quasi-symmetric spatial variation of the degree of alloying from the center to the edge of the flake. In general, the energy gap of an alloy A_xB_{1-x} in terms of the pure compound energy gap E_A and E_B, follows an equation[38]

$$E(x) = E_B + \left(E_A - E_B - b\right)x + bx^2 \quad (1)$$

where b is the bowing parameter. The variation of the band gap in a ternary semiconductor alloy as described by Equation 1 is found to be generally applicable in ternary 2D alloys as corroborated in previous studies.[18] The bowing parameter, b, in Equation 1 indicates the role of the confinement effects, among other factors, in constructing the band edges from two different metal atoms as in $Mo_xW_{1-x}S_2$ or non-metal atoms as in $MoS_{2(1-x)}Se_{2x}$.[39,40] For $Mo_XW_{1-X}S_2$ fitting PL peak positions to the above equation Chen et al,[23] obtained a b value of 0.25 eV for the A exciton peak and 0.19 eV for the B exciton peak. However, for the alloys $AB_{2(1-x)}C_{2x}$ where both B and C are chalcogen atoms, the bowing was found to be considerably smaller.[18] As the alloy composition is not directly determined in our samples, treating the scan position as a variable, and fitting the PL peaks in Figure 2f to the above equation gives a value of b ≈0.054 eV suggesting small bowing. From this, we surmise that the small bowing parameter indicates small lattice mismatch/strain and thermodynamic miscibility in our samples due to the unique CVD sample synthesis method employed in our study.

2.3. Low-Temperature Photoluminescence of the Alloyed Monolayer $Mo_xW_{1-x}S_2$

The excitation power dependence of the PL intensities provides insight into the nature of the radiative recombination processes that give rise to the different spectral features near the band edge at different regions of the alloyed structure.[41] To that end, we performed laser excitation power-dependent PL spectroscopy at low temperature (T = 4 K). **Figure 3a** shows the PL spectra of the $Mo_xW_{1-x}S_2$ alloy with data obtained at the W-rich edge region (region 3), Mo-rich center region (region 1), and the intermediate composition region (region 2) acquired using excitation laser power from in the range 2–200 μW. Throughout the paper, the PL spectra for all powers and the three regions were deconvoluted using six pseudo-Voigt function peaks shown in the shaded colored representative spectra, which provide the best fit of the experimental data (Figure 3a Peaks 2–5; peaks 1 and 6 are weaker compared to the other peaks and are not shown). Further representative spectra analysis is shown in Figure S1 (Supporting Information) at the edge, center, and intermediate composition regions using excitation laser power of 100 μW at 4 K.

2.3.1. Near Band Edge Peaks (1-3) in the Three Regions

In order to study the recombination mechanisms of different peaks in different regions of the alloyed $Mo_xW_{1-x}S_2$ monolayer, we have divided the fitted peaks into two main categories depending on their location relative to the band edges. First, we selected peaks close to the band edges (peaks 1–3), and then we chose peaks far away from those band edges (peaks 4–6). Figure 3b shows the peak positions for peaks 1–3 in three different regions of the alloyed monolayer as a function of excitation power to determine their origin. In the Mo-rich center region of the sample, the highest energy peak (peak 1 ≈ 2.01 eV) is weak for all the excitation powers. In this region, the position of peaks 1–3 shows negligible change with excitation power. For the intermediate MoW region, peaks 1–3 show a blue shift of ≈2 meV with increasing excitation power. This shift can be considered negligible as it is within the uncertainties of the spectral fitting. On the W-rich side, the peak shifts are larger, ≈4 meV for peak 1 and ≈9 meV for peak 2. Peak 3 shows initially a blue shift (≈9 meV) and then a red shift (≈4 meV). As the density of the photoexcited carriers increases with increasing excitation power, the quasi-Fermi levels for electrons and holes shift respectively into the conduction and valence bands leading to a blue shift.[42,43] However, other many-body interactions such as strain-induced band variation giving rise to reduced band gap and exciton binding energy would lead to a red shift of the excitonic peaks.[44,45] For the low excitation powers used in our experiments presumably the carrier density is not high enough to give rise to the many-body interactions, and the observed blue shifts are essentially caused by the shift of the quasi-Fermi levels.

To determine the physical origin of the different peaks in different regions of the alloyed semiconductor, power dependence of the integrated PL intensity of the various peaks is extracted. Figure 3c shows the PL intensity of peaks 1–3 as a function of excitation power using the power law $I = P^k$ fit where I, P, and k represent PL intensity, laser excitation intensity, and a numeric coefficient, respectively. Typically, free and bound excitons show a linear dependence of excitation power (k = 1), biexcitons show a quadratic dependence (k = 2), and sub-linear (k < 1) dependence would indicate the free-to-bound type of radiative transitions through impurities and defects.[46] The k values are indicated for the different peaks in Figure 3c. A three-particle center

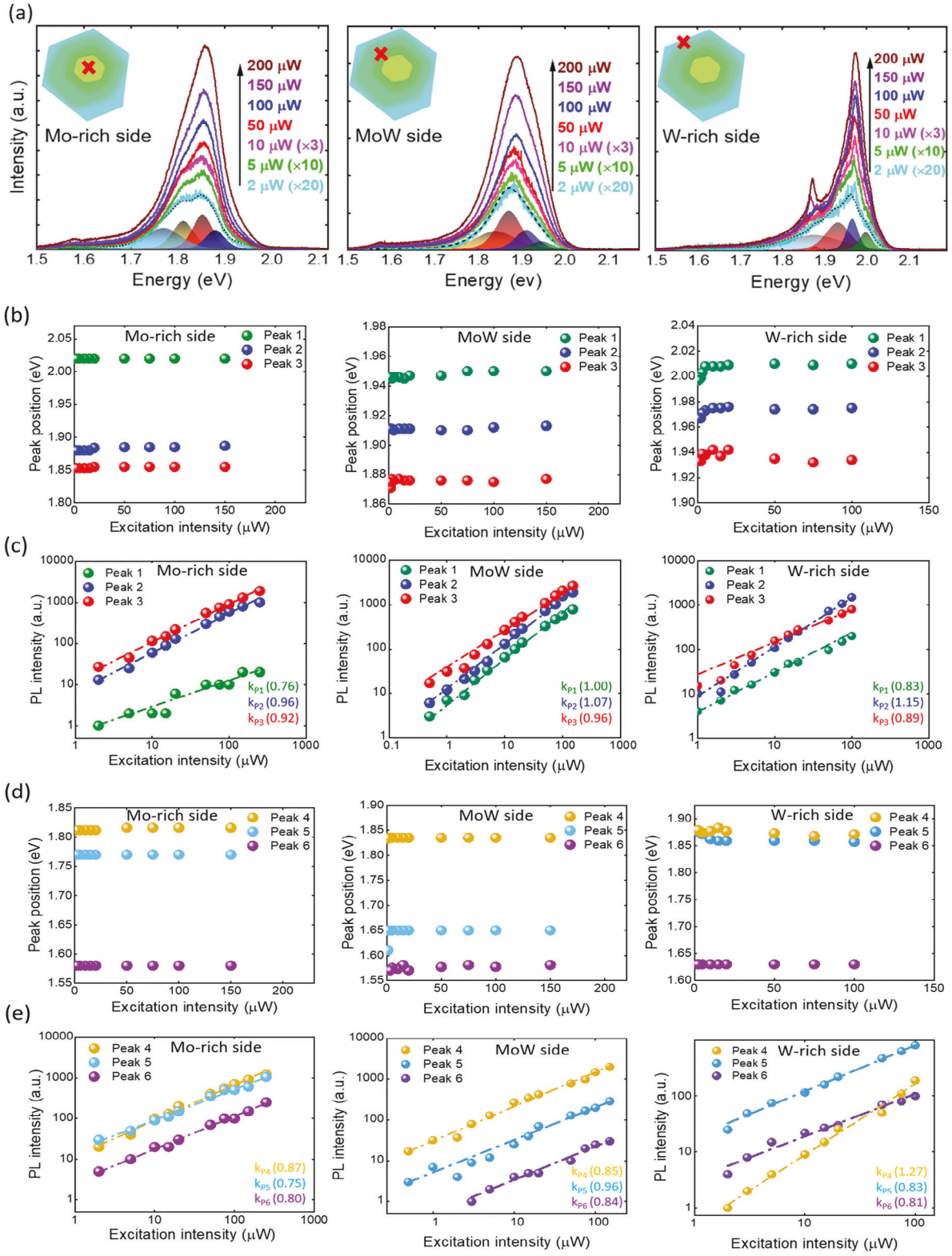

Figure 3. Laser excitation power dependence of the photoluminescence for the alloyed monolayer $Mo_xW_{1-x}S_2$ at T = 4 K. a) shows the spectra from the center (Mo-rich side), intermediate region (MoW side), and edge (W-rich side). b) Power dependence of the peak positions (peaks labeled 1–3) at the three regions. c) PL intensity of peaks 1–3 at different excitation powers at the three regions. d) Power dependence of peak position for peaks 4–6 at the three regions. e) PL intensity of peaks 4–6 at different excitation powers at the three regions.

like a trion would be expected to show a superlinear dependence (k = 3/2). However, if the trions dominate the radiative recombination process, which is likely at high excitation intensities, then a linear dependence (k = 1) is expected.[47] As evidenced in Figure 3c, peaks 1–3 show nearly a linear dependence on excitation intensity in all three regions. The low k value of 0.76 for peak 1 on Mo-rich side is attributed to the low PL intensity of the peak and the resultant uncertainties in the spectral fits. Based on the near linear dependence of the PL intensity on excitation intensity we surmise that the peaks 1–3 in all the regions are of excitonic origin.

By comparing the peak positions in the Mo-rich side of the $Mo_xW_{1-x}S_2$ alloyed monolayer with the values reported for the A and B excitons in monolayer pristine MoS_2 (Table S2, Supporting Information), we assign the peaks 1 (≈2.01 eV) and 2 (≈1.89 eV) in the Mo-rich side to the B and A excitons, respectively. Similarly, peak 1 in the W-rich side can be assigned to the A exciton. The B exciton in pristine WS_2 is generally much weaker than the A exciton and is rarely evidenced[48,49] in PL measurements. Accordingly, by comparing peak 1 in the W-rich region (≈2.01 eV) with the values reported for the A exciton in monolayer WS_2 (Table S1, Supporting Information), we assign it to the A excitonic transition in the W-rich side. Thus, the difference in the peak positions assigned to the A excitons on Mo-rich side and W-rich side is 120 meV which is comparable to the 100 meV PL shift observed at room temperature from center (Mo-rich side) to edge (W-rich side) (Figure 2c) in the $Mo_xW_{1-x}S_2$. As the band gap increases from the Mo-rich side to the W-rich side, the A excitonic position will increase continuously from the center to the edge region, we can assign peak 1 in region 2 (intermediate MoW side) to the A exciton. Thus, the A exciton peaks vary from 1.89 eV (Mo-rich side) to 1.95 eV (intermediate MoW side) and to 2.01 eV (W-rich side). Assuming similar exciton binding energies, this is consistent with the increase of the band gap going from MoS_2 to WS_2.

The near-linear dependence of the PL intensities of peak 3 (≈1.86 eV, region 1), and peaks 2 (≈1.91 eV, region 2) (≈1.98 eV, region 3) as shown in Figure 3c suggests they are of excitonic origin as well. Peak 3 (region 1) and peak 2 (regions 2 and 3) are separated from the respective A exciton peaks by 29 ± 2 meV in region 1, 36 ± 2 meV, and 33 ± 2 meV in regions 2 and 3, respectively. Generally, the PL peak observed on the low energy side of the A exciton in TMDCs is attributed to radiative recombination involving a three-particle (an exciton with an electron or a hole) trion,[43,50] with binding energies in the range of 20–40 meV in pristine MoS_2 and 40–60 meV in pristine WS_2 (Tables S1 and S2, Supporting Information). However, the expected k≈3/2 dependence on the excitation intensity of the assigned trion peak has not been reported.[47] Further, the calculated trion binding energies for MoS_2 and WS_2 are roughly the same, of the order of 30 meV, and are also very sensitive to the dielectric environment.[51] In an alloyed semiconductor such as $Mo_xW_{1-x}S_2$, the alloy disorder, if any, may also affect the trion binding energy. As shown in Figure 3c, peak 3 (region 1) and peak 2 (regions 2 and 3) show k = 1 suggesting an excitonic recombination. A previous study in monolayer WS_2 assigned the peak on the low energy side, separated by ≈29–35 meV from the A exciton to a bound excitonic transition.[36] We conclude that peak 3 (region 1) and peak 2 (regions 2 and 3) are not trion-related transitions but are bound exciton transitions arising from the same impurity or defect in the alloyed $Mo_xW_{1-x}S_2$. Over the range of excitation powers used, peak 3 in region 2 (≈1.88 eV) and region 3 (≈1.93 eV) are separated by 71 ± 2 and 69 ± 5 meV, respectively, from the A exciton peak. This peak also shows a linear dependence on excitation intensity implying a bound excitonic transition for its origin as well.

2.3.2. Peaks (4-6) far From the Band Edge in the Three Regions

As shown in Figure 3a, the PL spectra from $Mo_xW_{1-x}S_2$ show significant broadening on the low energy side in all three regions. The spectral fitting of this region yields three additional peaks, labeled P4, P5, and P6. The dependence of these peaks, observed far from the band edge, on excitation power is shown in Figures 3d,e. The peaks generally show negligible shifts in their positions with increasing excitation power with the exception of peak 5 (~ 1.88 eV @ 1 μW; 1.857 eV @ 100 μW) in the W-rich side which shows initially a red shift of ≈20 meV and saturates above 20 μW. It is expected in an alloy semiconductor that upon increasing the excitation intensity the photoexcited carriers migrate to regions of lower bandgap due to compositional grading before recombination. However, since the other peaks do not show such a large red shift, it is likely that peak 5 arises from a localized region of compositional disorder in region 3.

2.4. DFT Calculations

To assist in the analysis and assignment of the PL transitions observed at low temperatures, we performed DFT calculations to identify the role of alloying on the electronic band structure and in particular, on the energy levels of the predominant defect center, namely sulfur vacancy, V_S. Most theoretical work regarding the spin-orbit coupling effect in TMDCs considered pristine MoS_2 and WS_2, where the spin-orbit splitting between the spin-up and spin-down states in WS_2 and MoS_2 monolayers are calculated to be 0.4 eV[52,53] and 0.15 eV.[54–56] This splitting effect is largely responsible for the production of the A and B excitons in these pristine samples[57,58] (observed in PL spectra measurements due to spin-allowed bright excitonic transitions). While a few studies have used spin-orbit coupling for WS_2 and MoS_2 monolayers, there are not many studies involving the spin-orbit coupling effect with the V_S defect. When the V_S defect is considered, calculations reveal that the valence band splitting tends to decrease to 0.05 and 0.30 eV for both MoS_2[59,60], and WS_2[61] respectively. STM imaging of the V_S defect has confirmed the valence band splitting for WS_2 to be 0.25 eV[61] while only theoretical calculations have been shown to yield a decrease in valence band splitting for MoS_2 with the V_S defect. The V_S defect introduces defect levels within the bandgap, which are radiative and can be attributed to the origin of PL peaks below the A exciton.[36,62] Given that spin-orbit coupling has not been studied in $Mo_xW_{1-x}S_2$ alloys with varying Mo concentrations, this study attempts to both understand the evolution of the A and B exciton and the V_S defect-mediated radiative transitions by investigating multiple possible configurations for the $Mo_xW_{1-x}S_2$ alloy and examine how by varying the positions and concentration of W and Mo atoms surrounding the V_S defect affects the optical transitions.

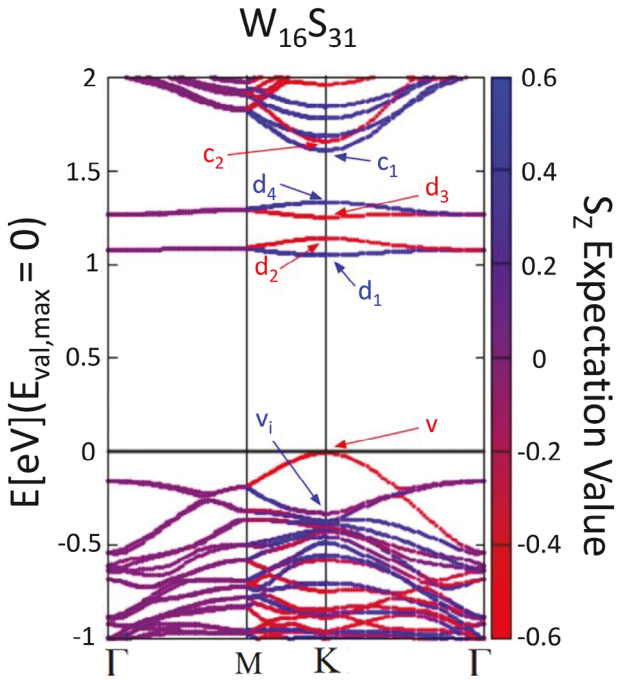

Figure 4. The $W_{16}S_{31}$ band structure was calculated using the PBE functional to illustrate the energy levels considered in the alloys. Note the spin-orbit split doublet structure of the VS level in the gap.

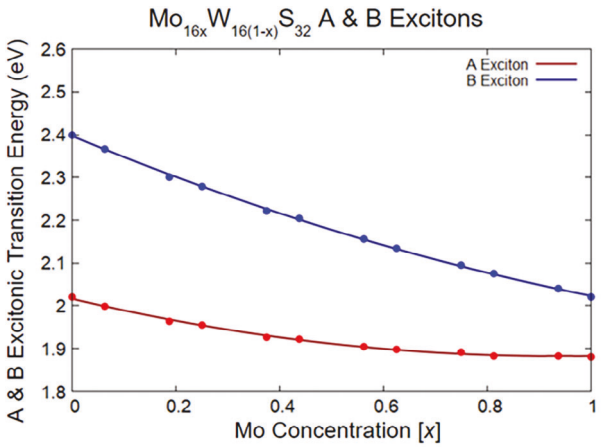

Figure 5. The evolution of the spin-down (A-exciton) and spin-up (B-exciton) vs Mo concentration [x] in pristine [$Mo_{16x}W_{16(1-x)}S_{32}$] alloys where the transition energies are shifted from the PBE functional exciton energies to the experimental exciton energies.

2.4.1. Sulfur Vacancy, V_S Levels (Computational Methods)

The energy levels are all considered at the K point with the distinct energy levels being denoted in the valence band, defect band, and conduction band (**Figure 4**) with $W_{16}S_{31}$ as an example. In all cases investigated, only the allowed transitions are considered. That is, the energy difference between bands of the same color (blue to blue and red to red) are allowed. The v-c_2 and v_i-c_1 transitions in the pristine alloys [$Mo_{16x}W_{16(1-x)}S_2$] are attributed to the A and B excitons, respectively. The defect-mediated transitions (v-d_2, v-d_3, v_i-d_1, and v_i-d_4) are obtained from the V_S hosting alloys [$Mo_{16x}W_{16(1-x)}S_2$] and are studied to develop a model to predict the transition energies based on the geometry of the alloy. In addition, the valence (v_i-v) and conduction band splitting (c_1-c_2) are also studied. For pristine $W_{16}S_{32}$ and $Mo_{16}S_{32}$, the A (B) excitonic transition energies are underestimated and are measured to be 1.607 eV (2.001 eV) and 1.615 eV (1.759 eV), respectively, with conduction (valence) band splitting of 0.032 eV (0.426 eV) and 0.003 eV (0.147 eV), respectively. Given the transitions are underestimated, a scissor shift is performed to correct the A (B) exciton energies to the experimental energies of 1.88 eV (2.02 eV) and 2.02 (2.40 eV) for $Mo_{16}S_{32}$ and $W_{16}S_{32}$, respectively.[63,64]

The evolution of the A exciton tends to decrease monotonically with the decrease in energy becoming less rapid as the Mo concentration [x] increases (**Figure 5**), which confirms the observations seen in the experimental PL spectra measurements (Figure 2; Tables S1 and S2, Supporting Information). The 32 configurations investigated in this study are divided into three separate classes based on the Mo concentration [x]: Mo-rich ($x \geq 0.75$), MoW [intermediate region] ($0.25 < x < 0.75$), and the W-rich ($x \leq 0.25$) regions. For each of these regions, the range of transition energies for each of the defect-mediated transition energies (R_1, R_2, B_1, and B_2 as shown in Figure S19, Supporting Information) for each of these three classes is shown in Table S4 (Supporting Information). In addition, since the defect levels tend to be significantly closer to the conduction band generating shallow defect levels when the V_S defect is surrounded by W atoms, a separate range is shown by separating the range of the transition energies obtained when the V_S defect is surrounded by Mo and W atoms to emphasize the possibility of V_S defects surrounded by W atoms contributing to the PL peaks below the A exciton[65,66] An example of this effect with the $Mo_{10}W_6S_{31}$ configurations is shown in Figure S21 (Supporting Information).

When the V_S defect is surrounded by W atoms, the ranges for the defect-mediated transitions match more closely to the P5 and P6 PL peaks observed in the experiment. Defect-mediated transitions associated with the d_2 and d_3 defect levels are assigned to the P5 and P6 PL peaks across the three distinct regions in **Table 1** and Table S4 (Supporting Information). From the excitation intensity of the PL intensities of P4–P6 shown in Figure 3e, it can be seen that most of the peaks show a sublinear dependence ($k < 1$) on excitation intensity with the exception of P4 showing a superlinear ($k > 1$) dependence in region 3 (W-rich side) and P5 showing a linear dependence $k \approx 1$) in region 2 (MoW side). While the peaks do not show a clear $k \approx ½$ dependence, the sublinear dependence may suggest their origin is due to free-to-bound type transitions. It is likely that in the spectral region away from the band edge the peaks may arise from both bound excitons and/or free-to-bound transitions arising from impurities/defects having energy levels within the gap of the alloyed semiconductor. Since the peaks away from the band edge should also follow the band gap increase from the Mo-rich side to the W-rich side of the $Mo_xW_{1-x}S_2$ alloyed monolayer, we can assign peak 4 (≈1.82 eV) in region 1 and peak 3 in region 2 and 3 (≈1.877 eV in region 2, 1.934 eV in region 3) to the same origin. The shift in the peak positions from region 1 to region 3 is ≈114 meV. Similarly, P4 in regions 2 and 3 (≈1.835 eV in region 2, 1.871 eV in region 3) and P5 in region 3 (1.857 eV) are conjectured to be of the same origin. P6 (≈1.6 eV) seen in all three regions appears to be band gap

Table 1. Peak assignments for the alloyed monolayer $Mo_xW_{1-x}S_2$, pristine MoS_2, and pristine WS_2 at T = 4 K.

Peak position assignment	Pristine MoS_2 [eV]	Pristine WS_2 [eV]	Mo-rich side of alloyed [eV] (Region 1)	MoW side of alloyed [eV] (Region 2)	W-rich side of alloyed [eV] (Region 3)
B-exciton	2.05	–	2.01 (P1)	–	–
A-exciton(X^0)	1.895	2.04	1.89 (P2)	1.95 (P1)	2.01 (P1)
Bound exciton $V_S^{BE}(d_3)$ (associated with V_S level, d_3, Figure 4) w/ exciton binding energy ≈20–36 meV[a)]	1.875	2.01	1.86 (P3)	1.913 (P2)	1.975 (P2)
Bound exciton transition $V_S^{BE}(d_2)$ (associated with V_S level, d_2, Figure 4) w/ exciton binding energy ≈70 meV[a)]	–	1.95	1.82 (P4)	1.88 (P3)	1.93 (P3)
Bound exciton/free-to-bound transition (unknown defect) (X^{BE})/(X^{FB}) w/ exciton binding energy ≈132 ± 7 meV[a)]	–	–	–	1.835 (P4)	1.871 (P4) 1.857 (P5)
Free-to-bound transition $V_S^{FB}(d_3)$ (associated with V_S level, d_3, Figure S19, Supporting Information)	1.73	–	1.77 (P5, R2)	1.65 (P5, R2)	1.63 (P6, R2)
Free-to-bound transition $V_S^{FB}(d_2)$ (associated with V_S level, d_2, Figure S19, Supporting Information)	1.68	–	1.58 (P6, R1)	1.58 (P6, R1)	–

[a)] Binding energy is defined as the energy separation of the peak from the A-exciton peak.[36]

independent. It should be noted that the P4–P6 peaks are not observed in the low temperatures' spectra from pristine monolayer WS_2 (see Figure S13, Supporting Information). Therefore, these features can be assumed to be caused by the presence of Mo in the $Mo_xW_{1-x}S_2$ alloyed monolayer.

Thus, based on the discussion above and the first principles calculation of the energy levels of the most likely point defect in alloyed $Mo_xW_{1-x}S_2$, namely, V_S, the following assignments of peaks in the different regions can be made as shown in Table 1. The various radiative recombination paths of peaks 1–6 in the three regions are illustrated in **Figure 6**. In the Mo-rich side peak 1 is marked as B-exciton (E_B). The peaks identified with bound excitons in all three different regions of the alloyed $Mo_xW_{1-x}S_2$ monolayer are shown with different binding energies (Δ) which are defined as the energy separation of the peak from the A-exciton peak (E_A). The free-to-bound transitions associated with V_S level, d_3 and d_2 as well as the unknown defect X are also shown in Figure 6a–c. The excitonic positions in a monolayer of pristine MoS_2 and WS_2 are summarized in Tables S1 and S2 (Supporting Information).

A broad band observed at ≈1.75 eV in monolayer MoS_2 similar to the P5 band in the Mo-rich region of the alloyed $Mo_xW_{1-x}S_2$ monolayer in our study has been identified with an exciton bound to ionized donor levels, related to V_S.[67] We assign the bands P5 and P6 in region 1 to a free-to-bound transition between the photoexcited electron captured at the V_S levels, d_3 and d_2, respectively, and a hole in the valence band. On the other hand, the peaks P3 and P4 in the Mo-rich region are identified with recombination through excitons bound to V_S levels, d_3 and d_2, respectively. The peaks P4 in region 2 (MoW side) and P4 and P5 in the W-rich region do not correspond to the calculated energy level positions of V_S and presumably arise from an unknown defect/impurity. It should be noted that P4 in the W-rich side is considerably sharper than P5. Further P4 shows a superlinear dependence on excitation intensity (k > 1) in region 3 while P5 has a sublinear (k < 1) dependence. It may be conjectured that in region 3, P4 and P5 arise from the same defect/impurity with the former being a bound exciton and the latter being a free-to-bound transition. In the intermediate MoW region, P4 may be a free-to-bound transition associated with the same defect/impurity. This defect/impurity is introduced as the W content increases.

2.5. Temperature Dependence of PL in Alloyed $Mo_xW_{1-x}S_2$

To further investigate the nature of excitons and the effect of the alloy in $Mo_xW_{1-x}S_2$, temperature dependent PL spectra were taken at different regions. **Figure 7a** depicts the evolution of PL spectra for three different regions of the alloyed $Mo_xW_{1-x}S_2$ monolayer in the temperature range 4–300 K. (A 532 nm excitation laser was used at a fixed power of 50 µW, and the laser exposure time was kept at 2 s for all spectra.) With increasing temperature, optical transition energies (peak positions) show a red shift as expected from the temperature dependence of the bandgap. The temperature dependence of the different peaks in the three regions of alloyed $Mo_xW_{1-x}S_2$ is shown in Figure 7b,c. We applied the O'Donnell equation[68] to fit the experimental peak positions near the band edge (peaks1–3) at different temperatures (dot dash-lines in Figure 7b) for all three regions of the alloyed monolayer $Mo_xW_{1-x}S_2$ as given by:

$$E_g(T) = E_g(0) - S\langle\hbar\omega\rangle\left[coth\left(\frac{\langle\hbar\omega\rangle}{2kT}\right) - 1\right] \quad (2)$$

where $E_g(0)$ is the ground-state transition energy at 0 K, S is a dimensionless coupling constant and $<\hbar\omega>$ is an average phonon energy, respectively. Table S3 (Supporting Information) shows the fitting parameters of peak positions at the different regions of the alloyed monolayer $Mo_xW_{1-x}S_2$. Based on the fitting the average phonon energy $<\hbar\omega>$ for A-exciton in pristine MoS_2, and in the Mo-rich side of the alloyed monolayer $Mo_xW_{1-x}S_2$ is 50 meV which is comparable to the reported values.[69,70] In addition, the

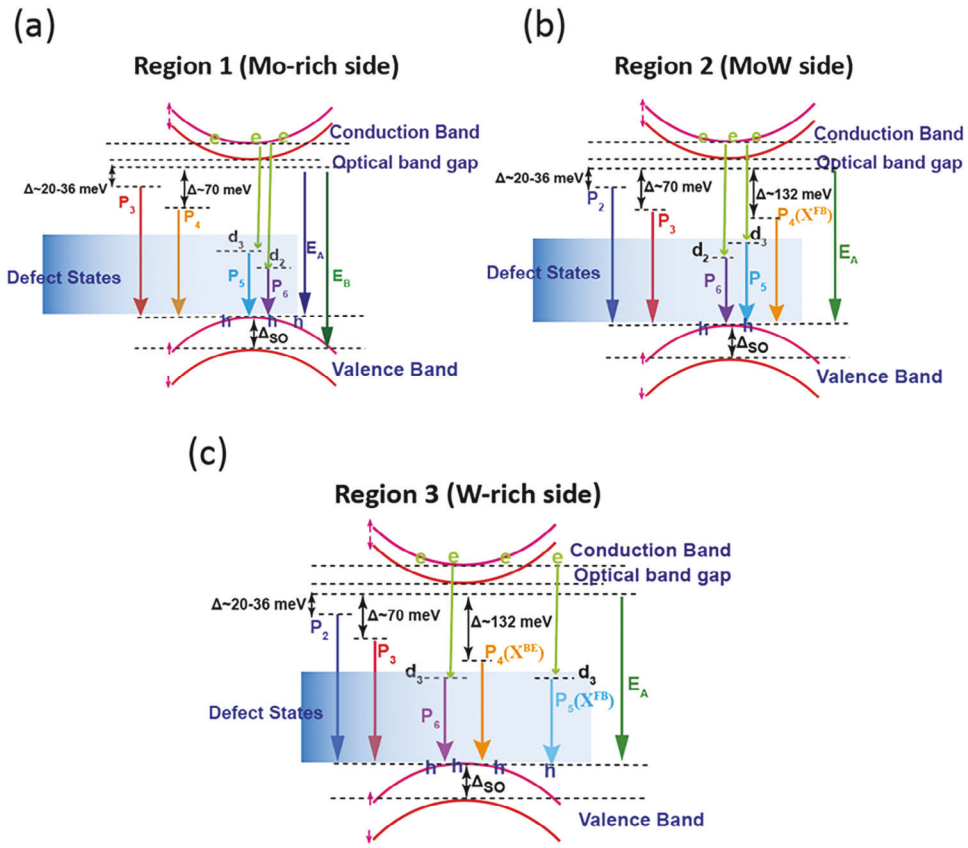

Figure 6. Various radiative recombination paths of peaks 1–6 at three regions of the alloyed $Mo_xW_{1-x}S_2$ monolayer. The energy band diagram is shown for a) the Mo-rich side, b) the intermediate MoW side, and c) the W-rich side of the alloyed $Mo_xW_{1-x}S_2$ monolayer. The bound exciton transitions through the doublet VS levels (d_3, d_2) are indicated as peaks P3 and P4 in Region 1, and P2 and P3 in Regions 2 and 3. The free-to-bound transitions through d_3 and d_2 are indicated by P5 and P6 in Region 1 and Region 2. The free-to-bound transition through d_3 in Region 3 is indicated by P6. The bound exciton through the unknown defect X is indicated by P4 in Region 3. The free-to-bound transition through the defect X is indicated by P4 in Region 2 and by P5 in Region 3.

average phonon energy $<\hbar\omega>$ for A-exciton (X^0) in both pristine WS_2 and W-rich side of the alloyed monolayer $Mo_xW_{1-x}S_2$ is ≈35–44 meV which is comparable to the reported values.[70,71] Based on Figure 7b the red-shift in the peak position of B-exciton in the Mo-rich side is ≈50 meV when the temperature increases from 4 to 300 K which is comparable with reported values.[72] The red shift for A-exciton in all three regions is about (≈33 ± 3 meV) when the temperature increases from 4 to 300 K.

The peaks assigned to bound excitons associated with the V_S levels d_3 and d_2 (see Table 1) are generally stable up to room temperature with the exception of the bound exciton associated with the d_2 level in region 1 (Mo-rich side) of the alloy which disappears above 100 K (Figure 7c). The peaks assigned to an unknown defect with a large exciton binding energy (132 ± 7 meV, Table 1) in regions 2 (intermediate region) and region 3 (W-rich side) persist at high temperatures, especially in the W-rich region of the alloyed $Mo_xW_{1-x}S_2$ monolayer (Figure 7c). The radiative transitions assigned to free-to-bound transitions involving V_S levels d_3 ($V_S^{FB}(d_3)$) are present even at room temperature. (See Figure S8, Supporting Information for a comparison of the PL spectra at low and high temperatures from the three regions). Interestingly, $V_S^{FB}(d_3)$ and $V_S^{FB}(d_2)$ transitions, are very prominent at low temperatures in pristine MoS_2 (see Figure S12, Supporting Information) and persist as a broad tail on the low energy side of the band excitons even at high temperatures. This observation suggests that the V_S levels dominate the radiative process in pristine MoS_2, especially at low temperatures. While the free-to-bound transitions via V_S levels dominate in pristine MoS_2, the bound excitons associated with V_S levels are observed in pristine WS_2 in the temperature range of 4–304 K (see Figure S13, Supporting Information). Thus, V_S plays an important role in the radiative processes in both MoS_2 and WS_2 as well as in the alloyed monolayer $Mo_xW_{1-x}S_2$. The dominance of either the free-to-bound transitions or the bound exciton transitions involving the V_S levels will be determined by the relative radiative rates of the transitions and the thermal ionization of the photoexcited electron from the V_S level, especially at high temperatures, which may differ between MoS_2 and WS_2 layers.

Figure 7d shows the integrated PL intensity versus the reciprocal of temperature near the band edge (peaks 1–3) in all three regions of alloyed monolayer $Mo_xW_{1-x}S_2$. The PL intensity (I_{PL}) decreases at high temperatures suggesting an Arrhenius type behavior.[11,69] The quenching of the free-to-bound transitions via the d_3 level of V_S (P5 in region 2 and P6 in region

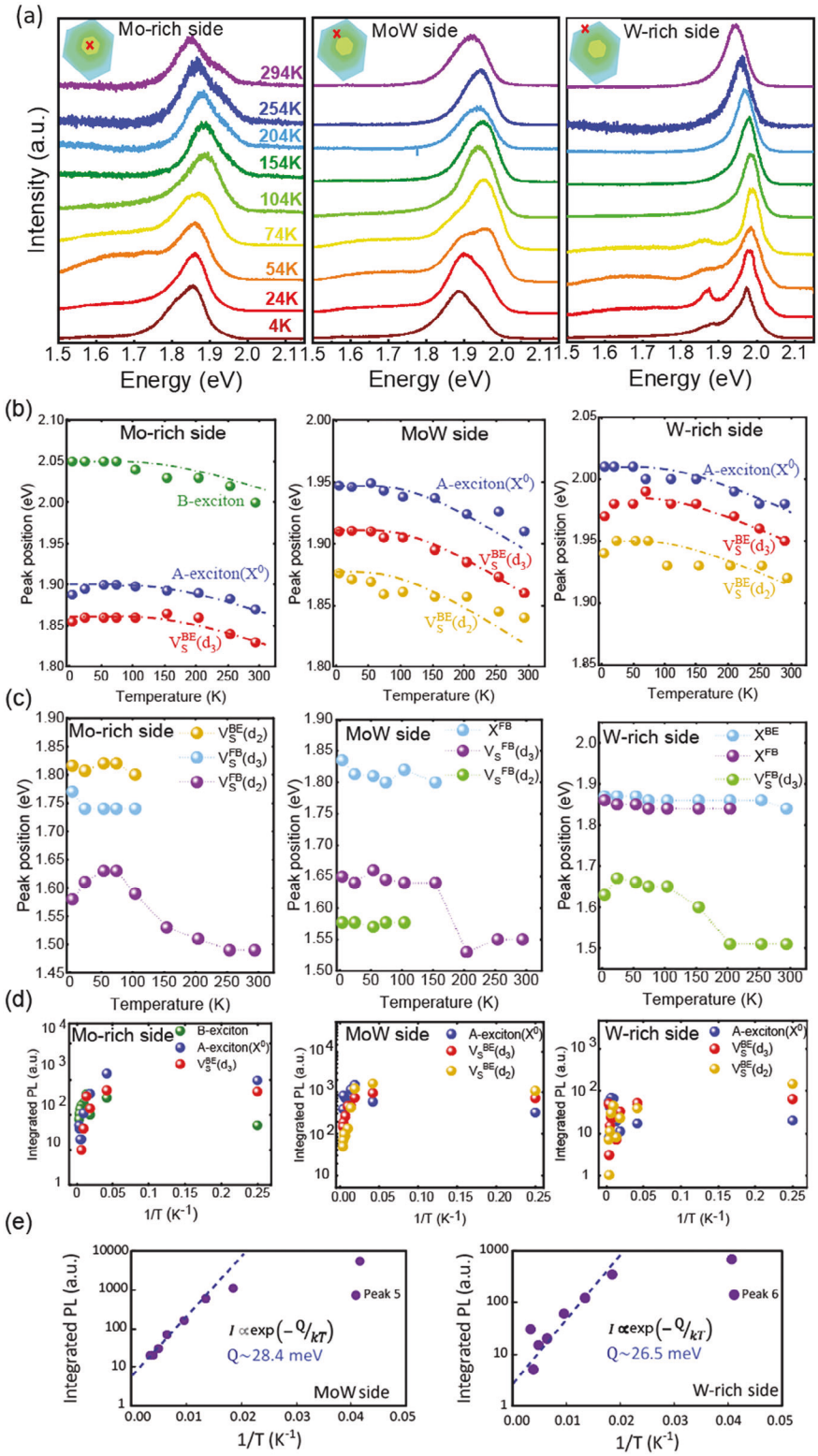

Figure 7. Evolution of PL Spectra of alloyed $Mo_xW_{1-x}S_2$ monolayer. a) shows PL Spectra as a function of temperature for alloyed structure in region 1 (Mo-rich side), region 2 (intermediate MoW side), and region 3 (W-rich side) of the flake. b) Evolution of peak position with temperature for 6 peaks at the three different regions of alloyed monolayer $Mo_xW_{1-x}S_2$. Dash-dot lines are calculated with the conventional temperature dependence of the semiconductor bandgap. d) Temperature dependence of the PL intensity for the near band edge peaks for alloyed $Mo_xW_{1-x}S_2$ monolayer. e) Temperature dependence of the PL intensity for peaks P5 and P6 from regions 2 (Intermediate MoW side) and 3 (W-rich side), respectively. Fitting an Arrhenius relation to the data yields an activation energy of 28.4 meV (P5) and 26.5 meV (P6).

3, Table 1) is shown Figure 7e. Fitting an Arrhenius relation $I_{PL} = const \times e^{\frac{Q}{KT}}$ to the data gives an activation energy Q≈26–28 meV. This value perhaps suggests the thermalization energy of the photoexcited electron captured at the d_3 level of V_S. A comparable activation energy of ≈36 meV was reported for PL emission associated with V_S in monolayer WS_2 and was attributed to the thermal dissociation of the bound exciton.[36]

The presence of V_S defects can influence the PL intensity. In regions with higher V_S defect density, we expect an increase in non-radiative recombination processes. As the non-radiative processes can be dominant at room temperature, we observe from the PL data in Figure S8 (Supporting Information) that the total PL intensity increases nearly by ≈4.9 times from the Mo-rich side to the W-rich side consistent with the decrease in S vacancy concentration in the latter region.

Figure S3 (Supporting Information) shows the FWHM versus temperature for the near band edge peaks (peaks 1–3) in the three regions of the alloyed $Mo_xW_{1-x}S_2$. It can be seen that the temperature dependence of FWHM could not be fitted to the equation describing the electron-phonon interaction (Equation S1, Supporting Information). The A-exciton peak is broader in regions 1 and 2 in comparison to region 3. The FWHM of the peaks associated with bound exciton transitions involving V_S levels are in the range of 60–80 meV. Compared to the pristine WS_2 and MoS_2, the changes of the FWHM for A-exciton (X^0) in region 1 and region 2 of the monolayer $Mo_xW_{1-x}S_2$ are larger than the changes of FWHM for pristine samples. For region 1 (Mo-rich side) of the alloy, it changes from 70 to 120 meV upon increasing the temperature from 4 to 300 K. However, for the pristine MoS_2 FWHM of the A-exciton changes from 38 to 50 meV (Figure S15, Supporting Information). For region 3 (W-rich side) of the alloy, it changes from 38 to 45 meV upon increasing the temperature from 4 to 300 K (Figure S3, Supporting Information). For pristine WS_2, the FWHM changes from 45 to 52 meV (Figure S15, Supporting Information) which is larger than the reported values for pristine MoS_2,[73] and pristine WS_2.[74]

The variation in V_S defect density also can affect the PL peak FWHM in alloyed $Mo_xW_{1-x}S_2$. Higher defect densities typically lead to increased inhomogeneous broadening. From Figure S3 (Supporting Information) it can be seen that at room temperature the FWHM decreases from 0.12 eV in the Mo-rich region to 0.08 eV in the interface, and to 0.045 eV in the W-rich region. Additionally, comparing the FWHM of the A exciton between the pristine samples and the alloyed sample, we observe that the FWHM for the A exciton increases compared to the pristine MoS_2 from 0.06 to 0.12 eV, while for WS_2 decreases slightly from 0.05 to 0.045 eV. These results indicate that the changes in the FWHM of the band edge optical transitions may be closely related to the S vacancy concentration.

3. Conclusion

In summary, using an alkali metal halide-assisted chemical vapor deposition approach, we successfully synthesized triangular TMDC alloy ($Mo_xW_{1-x}S_2$) monolayers with continuously varied W/Mo concentration from the center to the edges. The combined experimental photoluminescence characterization with theoretical DFT calculations including spin-orbit interactions enabled a thorough investigation of the nature of myriad intralayer optical transitions excitons in the alloyed monolayers. Aberration-corrected high-angle annular dark-field scanning transmission electron microscopy showed the presence of sulfur monovacancy, V_S, whose concentration varied across the graded $Mo_xW_{1-x}S_2$ layer as a function of Mo content with the highest value in the Mo rich center region. We identified free-to-bound transitions involving a photoexcited electron captured at the doublet V_S level and a hole in the top of the valence band by matching the calculated spin-allowed optical transition energies through a doublet V_S level in the gap. In addition, two bound exciton transitions associated with the V_S doublet were also identified. Further, the study of the temperature dependence of the photoluminescence helped to identify the differences brought about by alloying in comparison to the pure MoS_2 and WS_2 monolayers. Thus, a plethora of V_S related intralayer optical transitions reported for the first time in the alloy $Mo_xW_{1-x}S_2$, reveals the interplay between composition and defect structure. Our work highlights the capability of modulating the bandgap and engineering the defect structures simultaneously in 2D graded TMDC alloys via controllable synthesis strategies, and systematically studies how the optical transitions are modulated by the presence of structural defects.

4. Experimental Section

The Growth of Monolayer $Mo_xW_{1-x}S_2$ Alloys: To grow alloyed $Mo_xW_{1-x}S_2$ monolayers, powders of MoS_2 (≈5 mg), WO_3 (≈5 mg), and NaBr (≈0.5 mg) were mixed uniformly and placed inside a porcelain boat, and a piece of clean SiO_2/Si was placed on top of the boat with the polished side facing down. Note that the use of NaBr promoter can enhance the coverage of monolayers and increase the reproducibility of alloys. Subsequently, this porcelain boat was loaded into a one-inch quartz tube for CVD growth, and another porcelain boat containing sulfur powders (300 mg) was loaded upstream. In the growth process, the mixed MoS_2/WO_3/NaBr powders and the substrate were heated up to 825 °C and held for 10 min, and sulfur powders were heated up to 220 °C simultaneously for evaporation. Argon gas (100 sccm) was used as the carrier gas throughout the growth process and the growth was carried out at ambient pressure.

AC-HAADF-STEM: High-resolution aberration controlled HAADF-STEM images were taken using a FEI Titan3 G2 S/TEM operated at 80 kV and equipped with a double spherical aberration correction and monochromator. Images were acquired using a HAADF detector with a collection angle of 42–244 mrad, camera height of 115 mm, convergence angle of 30 rad, and a beam current of 50 pA. For the identification of sulfur mono-vacancies, AC-HRSTEM images were Fourier filtered using a low pass filter in the Digital Micrograph suite. In the same software, integrated intensity line scans were taken along the armchair direction, and the relative intensity of two overlapped sulfur atoms was used as a reference to identify sulfur mono-vacancies.

Optical Measurements: The power and temperature-dependent PL spectra were measured by the confocal laser scanning microscope system equipped with a vibration-free closed-cycle cryostat (Attodry 800, attocube). A 532 nm CW laser as an excitation source was focused into a small spot with a diameter of ≈2–3 µm on the sample through a 100 × objective lens (APO/VIS, N.A. = 0.82; attocube) inside the vacuum chamber. The PL spectra were then collected by the same lens and filtered the excitation signal by a 532 nm long-pass filter before entering a spectrometer (Andor) which consisted of a monochromator and a thermoelectrically cooled CCD camera. Room temperature hyperspectral PL was collected using AFM-assisted diffraction limited PL (neaspec co.) and recorded using a 328 mm focal length Andor spectrometer and imaged with a liquid nitrogen cooled silicon EMCCD camera (Andor iXon). The preliminary experiments were conducted to identify an optimal range of laser power—from

2 to 200 μW—which was critical to avoid any damage to the monolayer structure. Additionally, spatially resolved PL techniques were employed to uniformly scan different areas of the monolayer, ensuring that all the analysis accurately reflects the material's inherent optical properties.

DFT Calculation: The theoretical calculations were performed using Quantum Espresso (QE)[75] to aid in the interpretation of experimental results. The alloys were modeled using a hexagonal unit cell consisting of 3 atoms (either MoS_2 or WS_2) and were expanded to create a $4 \times 4 \times 1$ supercell consisting of 48 atoms with stoichiometry $Mo_{16x}W_{16(1-x)}S_{32}$ and varying Mo concentration (x). All calculations are performed using norm-conserving PBE[76] pseudopotentials[77] with the spin-orbit coupling (SOC) interaction included.[78] The lattice constant is set to $a = (3.183–0.002x)$ Å, which is based on the relaxed lattice constants of 3.181 Å for MoS_2 and 3.183 Å for WS_2. The force convergence threshold is set to 0.01 eV $Å^{-1}$, while the total energy threshold is set to 10^{-6} eV. Also, calculations are performed using a $2 \times 2 \times 1$ k-point mesh and the kinetic energy cutoff is 680 eV. The cell parameter in the z-direction is set to $c = 14.2$ Å to introduce a vacuum region and prevent undesired interactions between the monolayers. All possible alloy structures are constructed by substituting Mo and W atoms at the transition metal sites while preserving the C_{3v} symmetry. Assuming symmetry preservation, 32 possible alloyed structures can be generated in the $4 \times 4 \times 1$ supercell and the band structures for all 32 structures are determined both with and without a single V_S introduced (Figure S18, Supporting Information). All band structures are calculated using a Γ-M-K-Γ k-point path with the z-directional electronic spinor $\langle S_z \rangle$ also calculated to distinguish between spin up (blue) and down (red) states. From the calculated band structures, the various transitions at the K point are investigated to determine how the Mo concentration and geometry of the configuration affect these transitions.

Supporting Information

Supporting Information is available from the Wiley Online Library or from the author.

Acknowledgements

M.G. and Y.A. acknowledge support from the Air Force Office of Scientific Research (AFOSR) grant numbers FA9550-19-0252 and FA9550-23-1-0375. T.Z., D.Z., D.H., and M.T. acknowledge support from the AFOSR through grant No. FA9550-18-1-0072 and the NSF-IUCRC Center for Atomically Thin Multifunctional Coatings (ATOMIC). H.T. and Z.D.W. acknowledge funding support from the USA National Science Foundation (Award 2013640) and are grateful to the "Advanced Cyberinfrastructure Coordination Ecosystem: Services & Support" (ACCESS), which is supported by National Science Foundation grant number ACI-1548562 through proposal TG-DMR170008.

Conflict of Interest

The authors declare no conflict of interest.

Data Availability Statement

The data that support the findings of this study are available on request from the corresponding author. The data are not publicly available due to privacy or ethical restrictions.

Keywords

2D materials, alloying, photoluminescence, sulfur vacancy, transition metal dichalcogenides

Received: September 19, 2023
Revised: January 17, 2024
Published online: February 15, 2024

[1] A. Chaves, J. G. Azadani, H. Alsalman, D. R. da Costa, R. Frisenda, A. J. Chaves, S. H. Song, Y. D. Kim, D. He, J. Zhou, A. Castellanos-Gomez, F. M. Peeters, Z. Liu, C. L. Hinkle, S.-H. Oh, P. D. Ye, S. J. Koester, Y. H. Lee, P. Avouris, X. Wang, T. Low, *npj 2D Mater. Appl.* **2020**, *4*, 29.
[2] Y. Lei, T. Zhang, Y.-C. Lin, T. Granzier-Nakajima, G. Bepete, D. A. Kowalczyk, Z. Lin, D. Zhou, T. F. Schranghamer, A. Dodda, A. Sebastian, Y. Chen, Y. Liu, G. Pourtois, T. J. Kempa, B. Schuler, M. T. Edmonds, S. Y. Quek, U. Wurstbauer, S. M. Wu, N. R. Glavin, S. Das, S. P. Dash, J. M. Redwing, J. A. Robinson, M. Terrones, *ACS Nanosci Au* **2022**, *2*, 450.
[3] K. S. Novoselov, A. K. Geim, S. V. Morozov, D.-e. Jiang, Y. Zhang, S. V. Dubonos, I. V. Grigorieva, A. A. Firsov, *Science* **2004**, *306*, 666.
[4] S. Roy, X. Zhang, A. B. Puthirath, A. Meiyazhagan, S. Bhattacharyya, M. M. Rahman, G. Babu, S. Susarla, S. K. Saju, M. K. Tran, *Adv. Mater.* **2021**, *33*, 2101589.
[5] M. Ghafariasl, S. Singh, S. Gamage, T. Prusnick, M. Snure, Y. Abate, *Adv. Mater. Interfaces* **2023**, 2300794.
[6] S. Singh, M. Ghafariasl, H.-Y. Ko, S. Gamage, R. A. Distasio, M. Snure, Y. Abate, arXiv**2023**, arXiv:2306.17681.
[7] X. Yin, C. S. Tang, Y. Zheng, J. Gao, J. Wu, H. Zhang, M. Chhowalla, W. Chen, A. T. Wee, *Chem. Soc. Rev.* **2021**, *50*, 10087.
[8] D. Meng, M. Li, D. Long, Y. Cheng, P. Ye, W. Fu, E. Wentao, W. Luo, Y. He, *Comput. Mater. Sci.* **2020**, *182*, 109797.
[9] S. Zheng, L. Sun, T. Yin, A. M. Dubrovkin, F. Liu, Z. Liu, Z. X. Shen, H. J. Fan, *Appl. Phys. Lett.* **2015**, *106*, 063113.
[10] Y. Chen, W. Wen, Y. Zhu, N. Mao, Q. Feng, M. Zhang, H. P. Hsu, J. Zhang, Y. S. Huang, L. Xie, *Nanotechnology* **2016**, *27*, 445705.
[11] H. Li, X. Zhang, *Optical Materials* **2020**, *107*, 110150.
[12] S. Sharma, S. Bhagat, J. Singh, M. Ahmad, S. Sharma, *J. Mater. Sci.: Mater. Electron.* **2018**, *29*, 20064.
[13] H. J. Conley, B. Wang, J. I. Ziegler, R. F. Haglund Jr, S. T. Pantelides, K. I. Bolotin, *Nano Lett.* **2013**, *13*, 3626.
[14] F. Wang, S. Li, M. A. Bissett, I. A. Kinloch, Z. Li, R. J. Young, *2D Mater.* **2020**, *7*, 045022.
[15] J. Kang, S. Tongay, J. Li, J. Wu, *J. Appl. Phys.* **2013**, *113*, 143703.
[16] W. Tan, Z. Wei, X. Liu, J. Liu, X. Fang, D. Fang, X. Wang, D. Wang, J. Tang, X. Fan, *Sci. Rep.* **2017**, *7*, 15124.
[17] S. Susarla, A. Kutana, J. A. Hachtel, V. Kochat, A. Apte, R. Vajtai, J. C. Idrobo, B. I. Yakobson, C. S. Tiwary, P. M. Ajayan, *Adv. Mater.* **2017**, *29*.
[18] H. S. Kang, J. H. Kang, S. Lee, K. Lee, D. H. Koo, Y.-S. Kim, Y. J. Hong, Y.-J. Kim, K. Kim, D. Lee, C.-H. Lee, *NPG Asia Mater.* **2022**, *14*, 90.
[19] H. Li, X. Duan, X. Wu, X. Zhuang, H. Zhou, Q. Zhang, X. Zhu, W. Hu, P. Ren, P. Guo, L. Ma, X. Fan, X. Wang, J. Xu, A. Pan, X. Duan, *J. Am. Chem. Soc.* **2014**, *136*, 3756.
[20] Y. Gong, Z. Liu, A. R. Lupini, G. Shi, J. Lin, S. Najmaei, Z. Lin, A. L. Elias, A. Berkdemir, G. You, H. Terrones, M. Terrones, R. Vajtai, S. T. Pantelides, S. J. Pennycook, J. Lou, W. Zhou, P. M. Ajayan, *Nano Lett.* **2014**, *14*, 442.
[21] L. M. Xie, *Nanoscale* **2015**, *7*, 18392.
[22] Q. Feng, N. Mao, J. Wu, H. Xu, C. Wang, J. Zhang, L. Xie, *ACS Nano* **2015**, *9*, 7450.
[23] Y. Chen, J. Xi, D. O. Dumcenco, Z. Liu, K. Suenaga, D. Wang, Z. Shuai, Y.-S. Huang, L. Xie, *ACS Nano* **2013**, *7*, 4610.
[24] J. Jiang, N. Li, J. Zou, X. Zhou, G. Eda, Q. Zhang, H. Zhang, L.-J. Li, T. Zhai, A. T. Wee, *Chem. Soc. Rev.* **2019**, *48*, 4639.
[25] Y. H. Lee, X. Q. Zhang, W. Zhang, M. T. Chang, C. T. Lin, K. D. Chang, Y. C. Yu, J. T. W. Wang, C. S. Chang, L. J. Li, *Adv. Mater.* **2012**, *24*, 2320.

[26] J. Zhou, J. Lin, X. Huang, Y. Zhou, Y. Chen, J. Xia, H. Wang, Y. Xie, H. Yu, J. Lei, *Nature* **2018**, *556*, 355.
[27] T. Zhang, Voshell, A., Zhou, D., Ward, Z. D., Yu, Z., Liu, M., Aponte, K. O. D., Granzier-Nakajima, T., Lei, Y., Liu, H., Terrones, H., *Nanoscale* **2023**, *15*, 12348.
[28] T. Zhang, K. Fujisawa, F. Zhang, M. Liu, M. C. Lucking, R. N. Gontijo, Y. Lei, H. Liu, K. Crust, T. Granzier-Nakajima, *ACS Nano* **2020**, *14*, 4326.
[29] A. Fali, T. Zhang, J. P. Terry, E. Kahn, K. Fujisawa, B. Kabius, S. Koirala, Y. Ghafouri, D. Zhou, W. Song, *ACS Nano* **2021**, *15*, 2447.
[30] K. Bogaert, S. Liu, T. Liu, N. Guo, C. Zhang, S. Gradečak, S. Garaj, *Sci. Rep.* **2018**, *8*, 12889.
[31] Z. Lin, M. T. Thee, A. L. Elías, S. Feng, C. Zhou, K. Fujisawa, N. Perea-López, V. Carozo, H. Terrones, M. Terrones, *APL Mater.* **2014**, *2*, 092514.
[32] A. Azizi, Y. Wang, Z. Lin, K. Wang, A. L. Elias, M. Terrones, V. H. Crespi, N. Alem, *Nano Lett.* **2016**, *16*, 6982.
[33] H. Xu, J. Zhu, G. Zou, W. Liu, X. Li, C. Li, G. H. Ryu, W. Xu, X. Han, Z. Guo, J. H. Warner, J. Wu, H. Liu, *Nanomicro Lett* **2020**, *12*, 26.
[34] K. Bogaert, S. Liu, J. Chesin, D. Titow, S. Gradecak, S. Garaj, *Nano Lett.* **2016**, *16*, 5129.
[35] J. Hong, Z. Hu, M. Probert, K. Li, D. Lv, X. Yang, L. Gu, N. Mao, Q. Feng, L. Xie, *Nat. Commun.* **2015**, *6*, 6293.
[36] V. Carozo, Y. Wang, K. Fujisawa, B. R. Carvalho, A. McCreary, S. Feng, Z. Lin, C. Zhou, N. Perea-López, A. L. Elías, *Sci. Adv.* **2017**, *3*, e1602813.
[37] C.-S. Lee, G. Jin, S.-Y. Seo, J. Kim, C. Han, M. Y. Park, H. Ahn, S.-H. Lee, S. Cha, M.-H. Jo, *Chem. Mater.* **2020**, *32*, 5084.
[38] R. Hill, *Journal of Physics C: Solid State Physics* **1974**, *7*, 521.
[39] M. Zhang, J. Wu, Y. Zhu, D. O. Dumcenco, J. Hong, N. Mao, S. Deng, Y. Chen, Y. Yang, C. Jin, *ACS Nano* **2014**, *8*, 7130.
[40] J. Kang, S. Tongay, J. Li, J. Wu, *J. Appl. Phys.* **2013**, *113*, 143703.
[41] G. Gupta, S. Kallatt, K. Majumdar, *Phys. Rev. B* **2017**, *96*, 081403.
[42] A. Chernikov, C. Ruppert, H. M. Hill, A. F. Rigosi, T. F. Heinz, *Nat. Photonics* **2015**, *9*, 466.
[43] K. F. Mak, K. He, C. Lee, G. H. Lee, J. Hone, T. F. Heinz, J. Shan, *Nat. Mater.* **2013**, *12*, 207.
[44] A. Steinhoff, M. Rosner, F. Jahnke, T. O. Wehling, C. Gies, *Nano Lett.* **2014**, *14*, 3743.
[45] N. Peimyoo, J. Shang, W. Yang, Y. Wang, C. Cong, T. Yu, *Nano Res.* **2014**, *8*, 1210.
[46] T. Schmidt, K. Lischka, W. Zulehner, *Phys. Rev. B* **1992**, *45*, 8989.
[47] D. Kaplan, Y. Gong, K. Mills, V. Swaminathan, P. M. Ajayan, S. Shirodkar, E. Kaxiras, *2D Mater.* **2016**, *3*, 015005.
[48] W. Zhao, Z. Ghorannevis, L. Chu, M. Toh, C. Kloc, P.-H. Tan, G. Eda, *ACS Nano* **2013**, *7*, 791.
[49] H. M. Hill, A. F. Rigosi, C. Roquelet, A. Chernikov, T. C. Berkelbach, D. R. Reichman, M. S. Hybertsen, L. E. Brus, T. F. Heinz, *Nano Lett.* **2015**, *15*, 2992.
[50] C. Cong, J. Shang, Y. Wang, T. Yu, *Adv. Opt. Mater.* **2018**, *6*, 1700767.
[51] I. Kylänpää, H.-P. Komsa, *Phys. Rev. B* **2015**, *92*, 205418.
[52] M. Danovich, V. Zólyomi, V. I. Fal'ko, I. L. Aleiner, *2D Mater.* **2016**, *3*, 035011.
[53] H. Kahnouji, P. Kratzer, S. J. Hashemifar, *Phys. Rev. B* **2019**, *99*, 035418.
[54] A. Kormányos, V. Zólyomi, N. D. Drummond, G. Burkard, *Phys. Rev. X* **2014**, *4*, 011034.
[55] M. Zhong, C. Shen, L. Huang, H.-X. Deng, G. Shen, H. Zheng, Z. Wei, J. Li, *npj 2D Mater. Appl.* **2019**, *3*, 1.
[56] S.-D. Guo, *Comput. Mater. Sci.* **2016**, *123*, 8.
[57] Z. Li, T. Wang, S. Miao, Z. Lian, S.-F. Shi, *Nanophotonics* **2020**, *9*, 1811.
[58] J. G. Kim, W. S. Yun, S. Jo, J. Lee, C.-H. Cho, *Sci. Rep.* **2016**, *6*, 29813.
[59] Y. Wang, L. Deng, Q. Wei, Y. Wan, Z. Liu, X. Lu, Y. Li, L. Bi, L. Zhang, H. Lu, *Nano Lett.* **2020**, *20*, 2129.
[60] A. M. Z. Tan, C. Freysoldt, R. G. Hennig, *Physical Review Materials* **2020**, *4*, 064004.
[61] B. Schuler, D. Y. Qiu, S. Refaely-Abramson, C. Kastl, C. T. Chen, S. Barja, R. J. Koch, D. F. Ogletree, S. Aloni, A. M. Schwartzberg, *Phys. Rev. Lett.* **2019**, *123*, 076801.
[62] K. Wu, H. Zhong, Q. Guo, J. Tang, Z. Yang, L. Qian, S. Yuan, S. Zhang, H. Xu, *Adv. Opt. Mater.* **2022**, *10*, 2101971.
[63] Z. Li, Y. Xiao, Y. Gong, Z. Wang, Y. Kang, S. Zu, P. M. Ajayan, P. Nordlander, Z. Fang, *ACS Nano* **2015**, *9*, 10158.
[64] B. Zhu, X. Chen, X. Cui, *Sci. Rep.* **2015**, *5*, 9218.
[65] H. F. Haneef, A. M. Zeidell, O. D. Jurchescu, *J. Mater. Chem. C* **2020**, *8*, 759.
[66] M. A. Reshchikov, H. Morkoç, S. Park, K. Lee, *Appl. Phys. Lett.* **2001**, *78*, 2882.
[67] K. Greben, S. Arora, M. G. Harats, K. I. Bolotin, *Nano Lett.* **2020**, *20*, 2544.
[68] K. O'donnell, X. Chen, *Appl. Phys. Lett.* **1991**, *58*, 2924.
[69] N. Saigal, S. Ghosh, *Appl. Phys. Lett.* **2016**, *109*, 122105.
[70] J. Pandey, A. Soni, *Appl. Surf. Sci.* **2019**, *463*, 52.
[71] K. Wei, Y. Liu, H. Yang, X. Cheng, T. Jiang, *Appl. Opt.* **2016**, *55*, 6251.
[72] R. Sharma, J. Pandey, K. R. Sahoo, K. S. Rana, R. K. Biroju, W. Theis, A. Soni, T. N. Narayanan, *JPhys Mater.* **2020**, *3*, 045001.
[73] F. Cadiz, E. Courtade, C. Robert, G. Wang, Y. Shen, H. Cai, T. Taniguchi, K. Watanabe, H. Carrere, D. Lagarde, *Phys. Rev. X* **2017**, *7*, 021026.
[74] J. Krustok, R. Kaupmees, R. Jaaniso, V. Kiisk, I. Sildos, B. Li, Y. Gong, *AIP Adv.* **2017**, *7*, 065005.
[75] P. Giannozzi, S. Baroni, N. Bonini, M. Calandra, R. Car, C. Cavazzoni, D. Ceresoli, G. L. Chiarotti, M. Cococcioni, I. Dabo, *J. Phys.: Condens. Matter* **2009**, *21*, 395502.
[76] J. P. Perdew, K. Burke, M. Ernzerhof, *Phys. Rev. Lett.* **1996**, *77*, 3865.
[77] D. Hamann, *Phys. Rev. B* **2013**, *88*, 085117.
[78] A. Dal Corso, A. M. Conte, *Phys. Rev. B* **2005**, *71*, 115106.